RESEARCH ARTICLE | AUGUST 28 2024

Role of very large-scale motions in shock wave/turbulent boundary layer interactions

Jianhui Fan (范建辉) ; Jiaao Hao (郝佳傲) ; Chih-Yung Wen (温志湧)

Physics of Fluids 36, 086139 (2024)
https://doi.org/10.1063/5.0221601

Physics of Fluids **ARTICLE** pubs.aip.org/aip/pof

Role of very large-scale motions in shock wave/turbulent boundary layer interactions

Cite as: Phys. Fluids **36**, 086139 (2024); doi: 10.1063/5.0221601
Submitted: 2 June 2024 · Accepted: 8 August 2024 ·
Published Online: 28 August 2024

View Online Export Citation CrossMark

Jianhui Fan (范建辉), Jiaao Hao (郝佳傲), and Chih-Yung Wen (温志湧)[a]

AFFILIATIONS

Department of Aeronautical and Aviation Engineering, The Hong Kong Polytechnic University, Kowloon, Hong Kong

[a]Author to whom correspondence should be addressed: chihyung.wen@polyu.edu.hk

ABSTRACT

The present study investigates the cause of low-frequency unsteadiness in shock wave/turbulent boundary layer (TBL) interactions. A supersonic turbulent flow over a compression ramp is studied using wall-resolved large eddy simulation (LES) with a freestream Mach number of 2.95 and a Reynolds number (based on δ_0: the thickness of the incoming TBL) of 63 560. From the view of stability analysis, the effect of intrinsic instability on such low-frequency unsteadiness is excluded from the flow system by designing a ramp angle of 15°, and our attention is paid to the convective instability contributed by the incoming TBL. The LES results are analyzed by linear and nonlinear disambiguation optimization (LANDO), spectral proper orthogonal decomposition (SPOD), and resolvent analysis. The LANDO results reveal a streamwise scale-frequency relation of coherent structures in a very long (around $60\delta_0$) TBL, which indicates that the dynamics of very large-scale motions (VLSMs) in the TBL are featured by a low frequency. The SPOD results reveal that the most energetic SPOD mode features a low frequency that is identical to the dominant low frequency of the wall-pressure spectrum. Additionally, coherent structures of the mode resemble the VLSMs in the incoming TBL. These consistencies imply that the dynamics of VLSMs contribute to the low-frequency unsteadiness of the present flow. A resolvent analysis then further suggests that the origins of low-frequency dynamics of the present flow are from the VLSMs, which can be optimally amplified by the forcing in the turbulent flow.

I. INTRODUCTION

The interaction between a shock wave and a turbulent boundary layer (TBL) is commonly observed in high-speed flight vehicle components (such as air intakes and over-expanded nozzles). A strong interaction can lead to separated flow and low-frequency unsteadiness, which will result in adverse structural responses, such as aircraft structure buffeting, structural failure, and potential payload damage. Various physical mechanisms have been proposed to explain such unsteady motions,[1–3] but the cause of this unsteadiness remains an unresolved matter, subject to an ongoing debate.

The physical origins of the unsteady dynamics in shock wave/turbulent boundary layer interaction (STBLI) flows have been explored through flow instability analysis using theoretical and numerical techniques, such as global stability analysis (GSA) and resolvent analysis. Within the stability analysis community, two main mechanisms have been proposed: intrinsic and convective mechanisms. When considering laminar interactions, the dynamics of the shock wave/laminar boundary layer (SLBLI) system can be viewed as an oscillator or a noise amplifier.[4] For oscillator flows in SLBLI flows, the intrinsic mechanism has been observed in various studies of hypersonic compression-ramp flows,[5] oblique SLBLIs,[6–8] hypersonic double wedge flow,[9] and hypersonic double cone flow.[10] In these cases, GSA and direct numerical simulation (DNS) have been utilized to investigate the evolution of the perturbations in physical properties, such as spanwise wavelength. A consistent linear growth rate was observed between the most unstable mode identified by GSA and the temporal DNS history of the physical properties, indicating that the flow's early-stage unsteadiness arises from the intrinsic global instability. In contrast, for noise-amplifier flows in SLBLI flows, external disturbances are amplified through convective mechanisms, as demonstrated by the resolvent analysis conducted by Dwivedi *et al.*[11] and Hao *et al.*[12] The resolvent analysis reveals that the formation of streamwise streaks is a consequence of upstream disturbances being amplified. More recently, Hao[13] performed another resolvent analysis for globally stable STBLI flows. The highest responses in the analysis are illustrated to be caused by the modal resonance between the forcing and the leading global mode. A numerical simulation perturbed with the corresponding optimal forcing reveals that the response is in the form of a back-and-forth shock motion. Thus, while concerning turbulent interaction, as the turbulent perturbations of the incoming TBL can be regarded as one type of external disturbance acting on the separated flow,[14,15] it is believed that the structures within the incoming TBL are likely to make contributions to the dynamics of the STBLI flows in a convective way.

The present study focuses on the scenario of STBLI with an incipient separated flow where only the convective mechanism accounts for the low-frequency unsteadiness. Flow structures of the incoming TBL may play an important role in the unsteady dynamics of the subsequently separated flow. Several classes of flow structures exist in wall turbulence, which have been identified and characterized by both instantaneous visualizations and statistical quantities. Such structures include near-wall streaks, very large-scale motions (VLSMs), large-scale motions (LSMs), and hairpin packets.[16] Among these structures, the VLSMs are reminiscent of the superstructures observed in the work of Ganapathisubramani *et al.*[17] Note that we also refer to superstructures of external flows as VLSMs in the study. The superstructures present elongated regions of low and high speeds that extend to streamwise lengths greater than $30\delta_0$ (boundary layer thickness) in the logarithm region of incoming TBL. Ganapathisubramani *et al.*[17] also investigated the effects of these structures on separated flow dynamics by defining a separation line surrogate and relating it to fluctuations in the upstream boundary layer. A high correlation between upstream velocity fluctuations and the surrogate separation location in the incoming TBL is revealed. This high correlation is also observed in the work of Humble *et al.*[18] However, these observations of the superstructures are based on the extended flow field by applying Taylor's hypothesis, and the high correlation can provide only indirect evidence of the superstructures' contribution to the low-frequency unsteadiness of separated flow. The role of VLSMs (superstructures) in STBLI flows still needs to be clarified.

VLSMs have been identified in a variety of wall turbulent flows by experimental and numerical flow visualizations, as well as data-driven approaches. Most investigations on VLSMs have focused on their formations[19,20] and their influence on turbulence statistics.[21] Regarding the dynamics of VLSMs,[22–24] although the authors performed resolvent analysis for wall turbulence and showed and discussed typical VLSM-type motions in the response modes, the results based on its geometry model have limitations in explaining the unsteadiness of the separated flow. Additionally, according to our previous study on the dynamics of the turbulent boundary flow,[25] it is expected that there are VLSMs featured by low-frequency properties implied by a revealed relation that the streamwise scales of the coherent structures increase with the frequency decrease. However, the revealed relation has a limited frequency range because the computational domain in the previous study was insufficiently long in the streamwise direction. Thus, in the present study, a TBL flow featuring a very long streamwise distance is simulated to confirm the relation between the VLSMs and their low-frequency dynamics.

The content of the paper is organized as follows. Numerical configurations are described in Sec. II. The results of the large eddy simulation (LES) are presented in Sec. III. Analysis tools, which include linear and nonlinear disambiguation optimization (LANDO), spectral proper orthogonal decomposition (SPOD), and resolvent analysis, are applied in the study. The results obtained from these analysis tools are presented and discussed in Secs. IV–VI. Conclusions are given in Sec. VII.

II. COMPUTATIONAL DETAILS

The LES governing equations are the Favre-filtered Navier–Stokes equations (see our previous work[25]), and the subgrid-scale model applied in the governing equation is the dynamics Smagorinsky model. These LES governing equations are implemented in an in-house multi-block parallel finite-volume solver called PHAROS.[14,25–28] In this study, the advection upstream splitting method is utilized to calculate the inviscid fluxes, which are extended to the fifth order using the targeted essentially non-oscillatory scheme. The viscous fluxes are computed using the second-order central difference scheme. For time marching, a second-order implicit scheme is employed with a constant time step of $\Delta t = 20\,\text{ns}$.

Figure 1 depicts the schematic of the present ramp configuration. The freestream conditions of the present flow are $M_\infty = 2.95$, $T_\infty = 108\,\text{K}$, $\rho_\infty = 0.314\,\text{kg/m}^3$, $u_\infty = 614.6\,\text{m/s}$, and $Re_{\delta_0} = 63\,560$ taken from the experiment by Zheltovodov *et al.*[29] Note that $\delta_0 = 2.27\,\text{mm}$ is the thickness of the incoming turbulent boundary flow. The computational domain of the present flow is constructed by

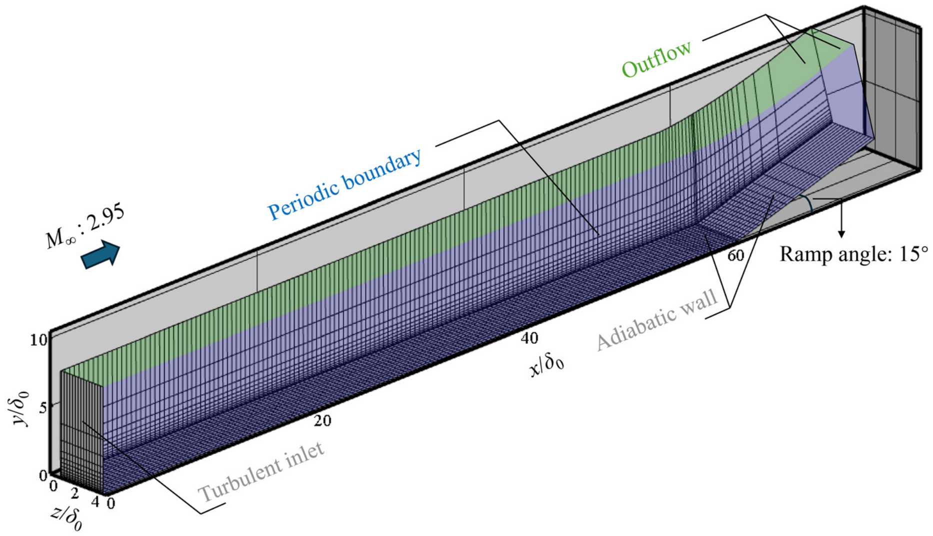

FIG. 1. Schematic of the compression-ramp configuration. The streamwise position of the corner of the model is $x/\delta_0 = 61.28$. Note that each of the tenth lines is shown along the *x*, *y*, *z* direction in the figure for the present mesh configuration.

extending the base grid (streamwise direction: 1601 × wall-normal direction: 131) along the spanwise direction (151 grid points) with the width of the spanwise domain of $L = 4\delta_0$. This mesh configuration features a very long computation domain (about 75 δ_0) in the streamwise direction, allowing us to capture the VLSMs in the flow field. The maximum wall-normal distance is about 18 δ_0 along the entire wall surface. The current setting of mesh then results in a $\Delta X^+ = 11.5$ and $\Delta Z^+ = 12.4$, which satisfies the grid-point requirement for LES simulation as suggested by Choi and Moin.[30] Additionally, the first point off the wall is approximately 3μm to maintain an initial wall-normal grid spacing in the inner units of $\Delta Y^+ = 0.66$. The notation ΔX^+ is defined as

$$\Delta X^+ = \frac{\rho u_\tau \Delta x}{\mu}, \tag{1}$$

where u_τ is the friction velocity, and the same definition also applies for ΔY^+ and ΔZ^+.

The boundary conditions are described as follows. The bottom boundary is a nonslip and adiabatic wall surface, including a flat plate and a ramp with a deflection angle of 15°. This angle gives a flow that is featured by a globally stable property. Note that, according to GSA results reported in the previous study,[13] the flow becomes globally unstable as the ramp angle is larger than an angle of about 23°. The inlet boundary conditions are set by utilizing the mean flow profiles from the corresponding experiment[29] with artificial turbulent fluctuations (generated by digital filter technique[31]) superimposed. The correlation properties of the artificial turbulent inflow are then examined by estimating the second-order correlation ($\boldsymbol{r}_{ij}$) and its correlation coefficient $\boldsymbol{R}_{ij}$ (autocovariance of the fluctuating velocity $\boldsymbol{u}_i'$), which are defined by

$$\boldsymbol{r}_{ij}(x,\eta,\tau) = \overline{\boldsymbol{u}_i'(x,\tau)\boldsymbol{u}_j'(x+\eta,t+\tau)}, \tag{2}$$

$$\boldsymbol{R}_{ij}(x,\eta,\tau) = \frac{\boldsymbol{r}_{ij}(x,\eta,\tau)}{\sqrt{\overline{\boldsymbol{u}_i'^2}(x)}\sqrt{\overline{\boldsymbol{u}_j'^2}(x+\eta)}}. \tag{3}$$

The overbar denotes time-averaging, while η and τ ($\tau = 0$ in this study) represent spatial and temporal separations, respectively. Figure 2 presents the three normal correlations ($i = j$) at the digital filter inlet and at a distance of $0.1\delta_0$ from the wall. The figure indicates that the artificial turbulent inflow can decorrelate rapidly to roughly zero $\boldsymbol{R}_{ij}$ over a very short streamwise distance (around $4\delta_0$), thereby not influencing the TBL statistics and the subsequent separated flow. The right and top boundary is the outflow boundary and is determined by using a simple extrapolation. Periodic boundary conditions are applied in the spanwise direction.

A two-dimensional (2D) solution is initially obtained using the Reynolds-averaged Navier–Stokes simulation to establish a base-flow solution. The initial flow field for the LES is constructed by duplicating the base-flow solution in the spanwise direction. Subsequently, the LES simulation is run for a time of $140\delta_0/u_\infty$ approximately to transient the initial flow field to the turbulent flow field. After that, the physical simulation time for the turbulent flow field is run up to approximately 3.6 ms ($974\delta_0/u_\infty$), which is sufficiently large to capture the low-frequency phenomenon. The sampling frequency is set as 1.0 MHz for data analysis.

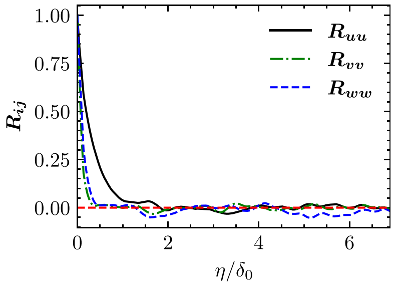

FIG. 2. Autocorrelation of velocity fluctuations in the streamwise direction at $y/\delta_0 = 0.1$ in the incoming boundary layer of the LES. The red dashed line is the zero correlation coefficient $\boldsymbol{R}_{ij}$.

III. LARGE EDDY SIMULATION OF THE PRESENT STBLI FLOW

Figure 3 shows one instantaneous flow field of the present flow. The grayscale plane contains the contour of the density gradient magnitude that shows flow structures such as a turbulent boundary layer (View 1) and a separated shock (View 2). An additional animation (Fig. 3, Multimedia view) is also given to show the unsteadiness of the separated shock. The wall surface shows the contour of the skin friction, which indicates the position of separation and reattachment. The wrinkled separation and reattachment lines can also be observed in the contour (View 3).

To validate our numerical results, Fig. 4 is given to show the wall-normal distribution of the mean profiles (streamwise velocity, temperature, density), Van Driest velocity,[32] and Reynolds stress by experimental data[29] (symbols in the figure) and LES results (curves in the figure) in the streamwise station of ($x/\delta_0 = 6.8$). Good agreement between experimental and numerical results can be observed in the figures, which confirms the credibility of the present LES results in the STBLI flow.

To examine the separation size of the present flow, the streamwise distribution of the spatial–temporal average skin friction (C_f) is obtained by LES results, as shown in Fig. 5(a). Here, C_f is defined by $\tau_w/0.5\rho_\infty u_\infty^2$, where τ_w is the wall shear stress. As read from the figure, the mean separation/reattachment values of the flow are located at $x/\delta_0 = 60.85$ and 61.45, respectively. The total length of the

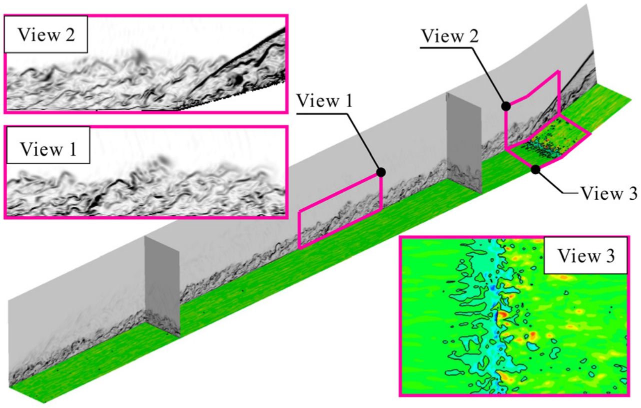

FIG. 3. Instantaneous flow field of the STBLI flow. The black curve in view 3 is the iso-line of zero skin friction. Multimedia available online.

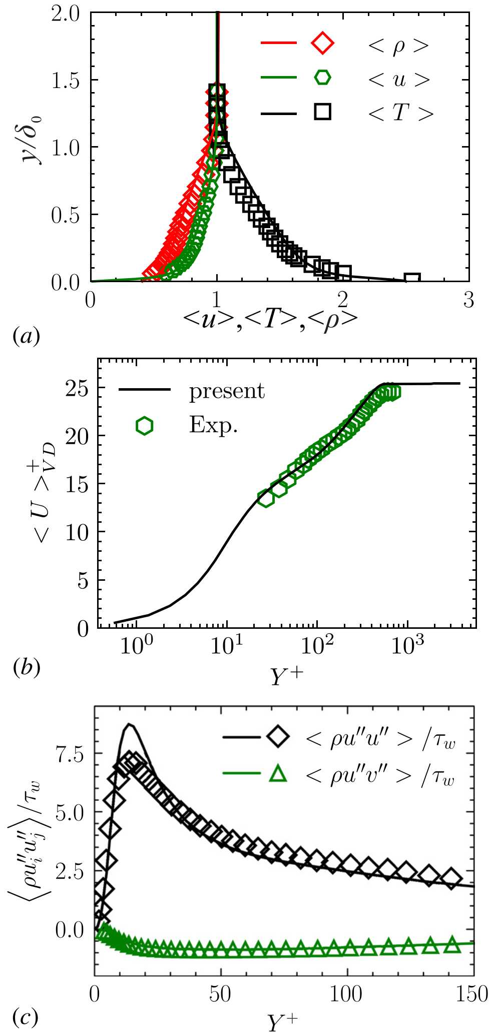

FIG. 4. Mean profiles of the incoming TBL at station $x/\delta_0 = 6.8$. (a) Profiles of the streamwise velocity, temperature, and density. (b) Profiles of the Van Driest velocity.[32] (c) Profiles of Reynolds stresses. The symbols are experimental results[29] and curves show the LES results.

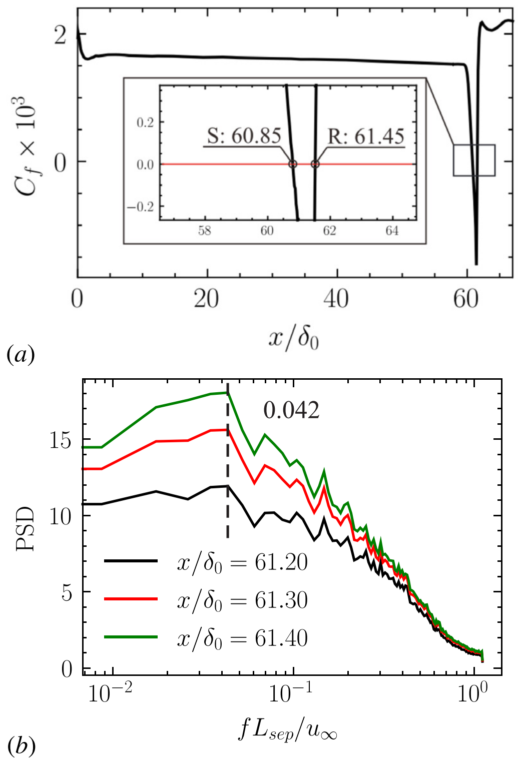

FIG. 5. (a) Distribution of the averaged skin friction along the streamwise direction. S and R denote the positions of separation and reattachment, respectively. (b) The power spectrum density of the wall pressure signal at $x/\delta_0 = 61.20$, 61.30, and 61.40.

separation size (L_{sep}) is then $0.6\delta_0$. Note that the location of the compression corner is at $x/\delta_0 = 61.28$.

To show the presence of the critical low-frequency unsteadiness of the present flow, the power spectrum density (PSD) of the spanwise-averaged wall-pressure signal at $x/\delta_0 = 61.20$, 61.30, and 61.40 (within the separation region) is shown in Fig. 5(b). The curves show a peak at a low frequency of about $fL_{sep}/u_\infty = 0.042$ (indicated by a dashed line in the figure). Note that the PSD curve is obtained by applying Welch's method with a segment size of 256 samples, 50 % overlap, and a Hamming window applied.

IV. LANDO ANALYSIS OF THE PRESENT FLOW

Frequently, the DMD technique, a frequency-orthogonal modal decomposition method, is employed to separate different dynamics from a broadband frequency spectrum for the present STBLI flow. The technique enables the extraction of essential information from individual frequency components in an unsteady flow field. The original dynamic system is decomposed into a set of reduced modes, where each mode corresponds to a distinct frequency behavior. The sum of these modes represents the overall dynamical system. However, the standard DMD method shows its challenge in dealing with the present STBLI flows that are featured by strong nonlinearity.[33] This feature can contaminate the mode estimate, causing the modes to be fragile. To overcome such concerns, LANDO[33] is introduced in the present study. The method can separate the linear and nonlinear contributions from the entire unsteady system as

$$\boldsymbol{Y} = \boldsymbol{L}\boldsymbol{X} + \boldsymbol{N}, \tag{4}$$

where $\boldsymbol{L}$ is the linear operation, $\boldsymbol{N}$ is the nonlinear forcing, and $\boldsymbol{X}$ is the input dataset. The technique involves training the input dataset, which comprises a series of time-series snapshots. A kernel learning method is utilized to derive the learning model f and the kernel model k for the dynamics system. Subsequently, using these models, an approximate linear operator $\boldsymbol{L}$ and a nonlinear forcing $\boldsymbol{N}$ can be determined. Both $\boldsymbol{L}$ and $\boldsymbol{N}$ are functions of model f and model k. The resulting $\boldsymbol{L}$ operator enables the extraction of a processed dataset that disregards the nonlinear component of the dynamical system. By utilizing this processed dataset, we can obtain a more physically interpreted decomposed mode by DMD. Details of the LANDO can be found in the work by

Baddoo *et al.*[33] Note that, as the formation of LSMs and VLSMs is related to a linear process,[34,35] in order to better visualize the organized motions, only the linear part of the dynamical system is considered to reconstruct the output dataset $\boldsymbol{Y}$ in the present study. The DMD analysis based on the processed dataset is then named the LANDO analysis, and the modes are named LANDO modes accordingly.

The present LANDO analyses contain two parts. The first part focuses on the physical domain of the separation region to illustrate the dominated low-frequency dynamics of the present STBLI flow, whereas the second part focuses on the domain of the incoming TBL. The dataset of the present LANDO analyses is constructed by $n = 3642$ snapshots of physic properties [e.g., spanwise-averaged density gradient magnitude, skin friction, and spanwise-averaged spanwise velocity (w)] with a time step of $1.0\,\mu$s. Only the linear part of the dynamics system is considered to reconstruct the dataset for the LANDO analysis. The current setup of the dataset results in a frequency resolution of $5.07 \times 10^{-4} < f\delta_0/u_\infty < 1.84$, which is sufficient to resolve the low-frequency phenomenon in the present study.

A. LANDO analysis of STBLI flow

Figures 6(a) and 7(a) show the magnitudes of the LANDO modes for density gradient magnitude and skin friction, respectively. The critical modes ϕ_c in the plots are selected due to the highest value among all decomposed modes. Both of these two critical modes feature a low frequency (fL_{sep}/u_∞) of about 0.04, which is consistent with the dominant frequency of PSD curves revealed in Fig. 5(b). Two animations [Fig. 6(b), Multimedia view, and Fig. 7(b), Multimedia view] are reconstructed (based on the ϕ_c) to show the critical flow motions for the present flow. The animation for the density gradient magnitude shows the oscillating motion of separated shock, while the animation for the skin friction illustrates the presence of unsteady elongated regions of surface streaks downstream the flow reattachment. In fact, these two dominant flow motions are also captured in our previous study,[25] which investigate the same flow conditions except that the ramp angle is 25°. In that study, the unsteady motion of separated shock is explained to be likely caused by a joint effect of global instability and the upstream disturbances, while the unsteady motion of surface streaks is the combined effect of the Görtler instability near flow reattachment and the convection of large-scale motions in the incoming TBL. A similar explanation can also be found in the work by Hao.[13] In that work, the strong similarities between the leading GSA mode and the optimal response of resolvent analysis for the supersonic flow over a compression ramp indicate a modal resonance between the forcing and the leading global mode, and an additional numerical simulation perturbed with the corresponding optimal forcing reveals that the response is in the form of an oscillating shock motion. All the above-mentioned findings suggest the importance of the forcing in the cause of the unsteady motions in STBLI flows. Thus, to understand how the forcing (turbulent fluctuation) contributes to the unsteady motions of the present STBLI flow, a study on the dynamics of the incoming TBL is necessary and constitutes the major work of the following content.

B. LANDO analysis of incoming turbulent boundary layer

Figure 8(a) shows the magnitudes of the LANDO modes, which are indicated by the stems in the plot. The red dashed curve is the PSD of the wall-pressure signal at streamwise $x/\delta_0 = 21.0$ (within TBL). The magnitudes of the leading LANDO modes follow the PSD curve within the frequency region smaller than roughly $fL_{sep}/u_\infty = 0.3$, whereas the magnitudes of the LANDO modes within the high-frequency region have relatively low values compared with the low-frequency components. This actually results from the treatments of LANDO, as high-frequency motions (such as small-scale motions of turbulent fluctuations) in TBL are characterized by strong nonlinearity, which is primarily eliminated from the current LANDO analysis. Four of the energetic LANDO modes for the averaged spanwise velocity are then selected and shown in Fig. 8(b). These modes are selected to show coherent structures with different streamwise wavenumbers within a wide frequency range. Note that, due to the high ratio of the streamwise distance to the boundary thickness of the figure, the presented LANDO modes (also the following SPOD modes and resolvent modes) are not to scale to better show the feature of coherent structures. A trend can be observed that the streamwise wavelength of the coherent structures increases as the frequency decreases. The streamwise scale of the coherent structures (Γ/δ_0) is then estimated according to LoD/n, where n is the estimated number of coherent structures of the captured modes, and LoD is the length of the domain of the captured modes, which is ($50\delta_0$) in the present study. We then plot these data in the frequency-scale diagram, as shown in Fig. 9, and a fitted curve is obtained by performing a nonlinear regression. As revealed by the fitted curve, there exists a relation between the frequency and the streamwise scale of the coherent structures that satisfies

$$\Gamma = 0.78u_\infty/f. \tag{5}$$

Note that as the relation is captured from LANDO, it only suggests the dominant dynamics of organized motions in TBL.

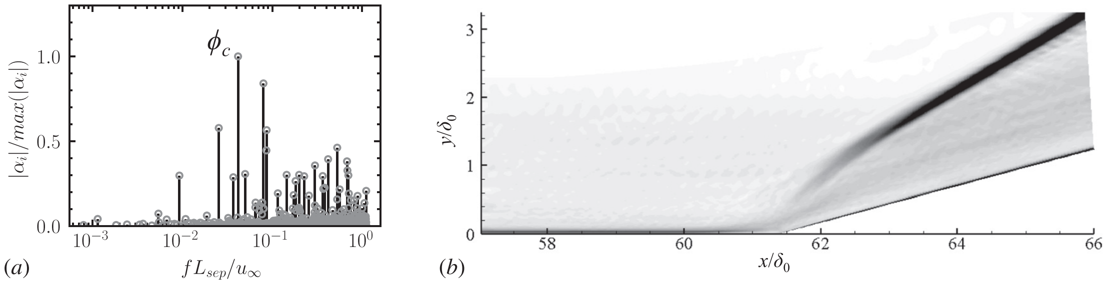

FIG. 6. (a) The magnitude of the LANDO modes for the density gradient magnitude. α_i is the amplitude of the LANDO mode ϕ_i. (b) Reconstructed animation based on the critical LANDO mode of ϕ_c. Multimedia available online.

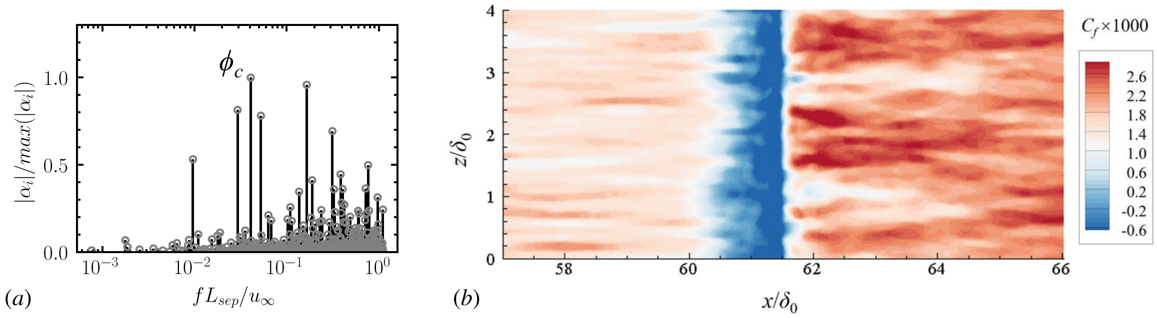

FIG. 7. (a) The magnitude of the LANDO modes for skin friction. α_i is the amplitude of the LANDO mode ϕ_i. (b) Reconstructed animation based on the critical LANDO mode of ϕ_c. Multimedia available online.

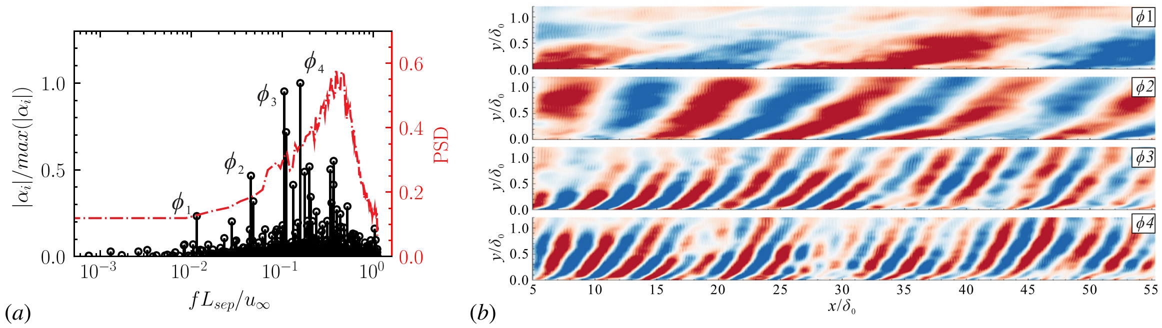

FIG. 8. (a) The magnitude of the LANDO modes for the spanwise velocity. α_i is the amplitude of the LANDO mode ϕ_i. The red dashed curve is the PSD of the wall pressure signal at streamwise $x/\delta_0 = 21.0$ (within TBL). (b) Coherent structures of LANDO modes of the averaged spanwise velocity for mode ϕ_1–ϕ_4: $fL_{sep}/u_\infty = 0.011, 0.045, 0.11, 0.16$, respectively. The contour levels are evenly spaced between ± 0.25 of the maximum fluctuation.

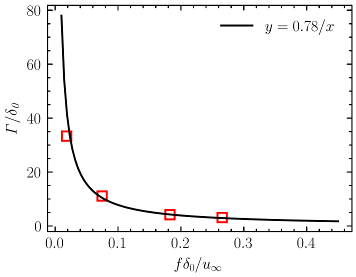

modes	ϕ_1	ϕ_2	ϕ_3	ϕ_4
n	1.5	4.5	12.0	16.0
$\Gamma/\delta_0 = LOD/n$	50/1.5	50/4.5	50/12.0	50/16.0
$f\delta_0/u_\infty$	0.018	0.075	0.183	0.266

Estimated scale of the coherent structures in the TBL

FIG. 9. Estimated streamwise scale of coherent structures as a function of the frequency of LANDO modes.

The above findings show some significance for the dynamics of the incoming TBL. First, VLSMs in the wall turbulent flow are believed to feature very low-frequency dynamics according to the scale-frequency relation, which is likely to account for the low-frequency unsteadiness of STBLI flows. Second, these dominant motions (VLSMs and LSMs) propagate at a constant velocity along a streamwise direction with $U_c = 0.78\,u_\infty$. The constant convective velocity is reminiscent of the recent work conducted by Zhu *et al.*[36] In their work, they showed that the most energetic resolvent mode at a certain wall-normal location in an incompressible turbulent boundary layer maintains a constant convective speed ($0.86u_\infty$ in their work). In addition, Zhou *et al.*[37] also reported that two hairpin structures (primary and downstream) propagate at approximately the same convection velocity, which is identified by the central peak of the cross correlation diagram. The convective velocity is 72 % of the centerline velocity of the turbulent pipe flow, which is nearly consistent with the velocity revealed by the fitted curve. These critical convective velocities for large-scale structures support the hypothesis that LSMs and VLSMs are created by the vortex packets formed when multiple hairpin structures travel at the same convective velocity.[16,38]

V. SPOD ANALYSIS OF THE PRESENT STBLI FLOW

Another data-driven technique applied in the present study is SPOD.[39] The method can determine and rank orthogonal modes with a given dataset, thereby optimally accounting for the statistical variability of turbulent flows. In other words, SPOD modes are able to represent dynamically important coherent structures and optimally account for the random nature of the present STBLI flow.

A brief introduction of the SPOD algorithm is described as follows. Decomposing the time-series snapshots of perturbation $\boldsymbol{X}'$ by discrete Fourier transform in temporal dimensions gives the decomposed data matrices, $\boldsymbol{D}_\omega$. A spectral density, $\boldsymbol{P}_\omega$, is then available by multiplying the decomposed matrices and their complex conjugate (denoted by a superscript $*$) at a particular frequency

$$\boldsymbol{P}_\omega = \boldsymbol{D}_\omega \boldsymbol{D}_\omega^*, \tag{6}$$

to which we solve the SPOD eigenvalue problem presented by Lumley[40,41]

$$\boldsymbol{P}_\omega \boldsymbol{W} \Psi_\omega = \Psi_\omega \Lambda_\omega, \tag{7}$$

where $\boldsymbol{W}$ is the weight matrix. The SPOD mode forms from the columns of Ψ_ω, ranked by the diagonal matrix of eigenvalues $\Lambda_\omega = \mathrm{diag}(\lambda_1, \lambda_2, \ldots, \lambda_N)$. The modes are orthogonal in the energy norm estimated by Chu energy[42] and satisfy $\Psi_\omega^* \boldsymbol{W} \Psi_\omega = \boldsymbol{I}$. As a result, the expansion of the spectral density tensor gives

$$\boldsymbol{P}_\omega = \Psi_\omega \Lambda_\omega \Psi_\omega^*. \tag{8}$$

Details of the SPOD algorithm are also available in the works of Taira *et al.*[39]

The dataset of the present SPOD is the collection of the spanwise-averaged spanwise velocity (w) with a number of snapshots of 3642. The configuration of the SPOD computations has a hamming window and block sizes of 256 snapshots with a 50 % overlap, resulting in 27 independent blocks. The computation domain covers the range $5.0 < x/\delta_0 < 66.0$ and $0.0 < y/\delta_0 < 4.5$ for the spanwise-averaged LANDO analysis, which includes the incoming TBL and the following separated flow.

Figure 10(a) shows the SPOD eigenvalue spectrum of the spanwise-averaged component (w) of the present flow. The vertical axis E stands for modal energy, and each curve identifies how the modal energy changes as a function of frequency (similar to traditional PSD curves). In the figure, the blue-shaded region highlights the gap between the first and second modes. A substantial gap indicates that the primary mode holds significantly more energy compared to the others. A larger separation signifies the dominance of the leading modes, resulting in the flow exhibiting behavior of lower rank.

By examining the figure, it can be seen that the spectra of λ_1 (the most energetic curve) have their peaks at approximately $fL_{sep}/u_\infty = 0.042$, which is consistent with the critical peak frequency in the wall-pressure spectrum of Fig. 5(b). The peaks of the eigenvalue spectra imply the most energetic SPOD mode of the present flow, which is then shown in Fig. 10(b). As indicated in the figure, the mode features very large-scale coherent structures with a streamwise scale of approximately $12.0\,\delta_0$, which is almost identical to the scale of the LANDO mode ϕ_2 shown in Fig. 8. It is also worth noting that the SPOD mode's critical scale $(\Gamma = 12.0\,\delta_0)$ and frequency $(fL_{sep}/u_\infty = 0.042)$ can result in coherent structures' convective velocity of approximately $0.8\,u_\infty$, which is nearly the same as that of the revealed relation (5) shown in Sec. IV. Additionally, the SPOD results also reveal that the low-rank behavior is apparent over the frequency fL_{sep}/u_∞ values smaller than 0.3, where LSM and VLSMs are prevalent in TBL, as revealed by previous LANDO results. Thus, the low-rank behavior and the optimal SPOD mode suggest that the VLSMs may play an important role in the low-frequency dynamics of the STBLI flow.

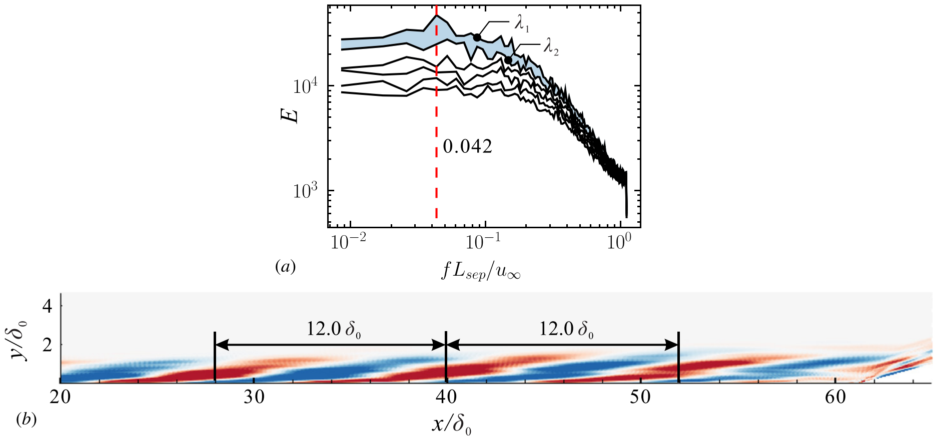

FIG. 10. (a) SPOD eigenvalue spectra for the present STBLI flow. Only six leading spectra (λ_{1-6}) are shown in the figure. (b) The most energetic SPOD mode of the averaged spanwise velocity with $fL_{sep}/u_\infty = 0.042$. The contour levels are evenly spaced between ±0.25 of the maximum fluctuation.

VI. RESOLVENT ANALYSIS OF THE PRESENT STBLI FLOW

To further confirm the view that VLSMs account for the low-frequency unsteadiness in the present STBLI flow, resolvent analysis is performed. We are going to observe the response of the base flow to an input forcing with a wide range of frequencies. To achieve that, a forcing term $\boldsymbol{f}'$ is added to governing equations of perturbation (derived by adding small perturbation into the Favre-filtered Navier–Stokes equation) as

$$\frac{\partial \boldsymbol{U}'}{\partial t} = \boldsymbol{A}\boldsymbol{U}' + \boldsymbol{B}\boldsymbol{f}', \tag{9}$$

where matrix $\boldsymbol{A}$ is the 2D Jacobian matrix that depends only on the base flow, and matrix $\boldsymbol{B}$ constrains the forcing to a localized region. The turbulent eddy viscosity μ_T applied in matrix $\boldsymbol{A}$ is obtained based on the Boussinesq hypothesis, which was described in detail in the work.[25] The forcing and response are assumed to be harmonic in time and in the spanwise direction as

$$\boldsymbol{f}'(x,y,z,t) = \hat{\boldsymbol{f}}(x,y)\exp(\mathrm{i}\beta z - \mathrm{i}\omega t), \tag{10}$$

$$\boldsymbol{U}'(x,y,z,t) = \hat{\boldsymbol{U}}(x,y)\exp(\mathrm{i}\beta z - \mathrm{i}\omega t). \tag{11}$$

Substituting (10) and (11) into (9) results in

$$\hat{U} = \boldsymbol{R}\boldsymbol{B}\hat{f}, \quad \boldsymbol{R} = (-\omega \boldsymbol{I} - \boldsymbol{A})^{-1}. \tag{12}$$

Here, matrix $\boldsymbol{R}$ is the resolvent matrix, and matrix $\boldsymbol{I}$ is the identity matrix. We are interested in finding the forcing and response that maximize the energy amplification (often referred to as the gain). In this study, the gain G is estimated by the ratio of the Euclidean norm of Chu energy and the corresponding maximum value in the flow field. Additionally, to find the optimal gain, an eigenvalue problem is solved by using the power iteration. Readers may refer to our previous work[12,25] for more details of the framework of resolvent analysis.

The base flow for the present resolvent analysis is the spatial–temporal averaged LES flow field on the $x - y$ plane. The computation domain covers the $5.0 < x/\delta_0 < 66.0$ and the entire y range, resulting in a cell size of 1510 (streamwise direction) × 130 (wall-normal direction). Note that the verification of grid independence for resolvent analysis is provided in the Appendix, which suggests that the present mesh configuration is sufficient for the present resolvent analysis. The present resolvent analysis is conducted over a range of spanwise wavenumbers (βL ranges from 0.1 to 0.8) and angular frequencies ($\omega L/u_\infty$ ranges from 0.10 to 0.24). The applied forcing is localized slightly downstream of the inlet boundary at a location of $x/\delta_0 = 8.0$. The resulting optimal gain is premultiplied as

$$G_w = \log_{10}\left(\beta L * \frac{\omega L}{u_\infty} * G^2\right), \tag{13}$$

where L is the reference length, which is 1 mm in the present study.

Figure 11 shows the distribution of premultiplied optimal gain. The solid curves show the distributions of G_w as a function of the spanwise wavenumber at one specific angular frequency. The diamonds are the optimal G_w for each solid curve. Among these optimal gains, the diamonds are highlighted as red by a criterion that G_w is larger than 0.99 maximum G_w. The frequency of these optimal gains ranges from 0.14 to 0.20 ($\omega L/u_\infty$) or, equivalently, 0.030 to 0.043 for fL_{sep}/u_∞. This range includes the dominant frequency of the PSD curve shown in Fig. 5(b), although the dominant frequency is located at a position close to the right boundary of the range. The slight shift of the dominant frequency of PSD from that of the maximum G_w is reasonable. Results of the resolvent analysis are based on the linear theory, whereas the PSD result is obtained directly from the natural STBLI flows. Nevertheless, the distribution of the premultiplied optimal gain suggests that the observed dominant (low frequency) unsteadiness in the STBLI flows can be regarded as an optimized response to the turbulent fluctuations (input forcing) from the incoming boundary layer, specifically, to the energetic motions of TBL.

Four resolvent modes R1–R4 (see Fig. 11) are selected and examined in the present study as shown in Fig. 12, which have nondimensional frequencies ($\omega L/u_\infty$) of 0.14, 0.16, 0.18, and 0.20, respectively. It is noted that the revealed streamwise scale-frequency relation (5) in Sec. IV is also valid for the coherent structures of the response modes. This is suggested by the fact that, with the relation and known frequencies, the streamwise scale of the coherent motions is estimated as 15.4 δ_0, 13.5 δ_0, 12.0 δ_0, and 10.8 δ_0, which are almost identical to that of resolvent modes R1–R4 calculated by the framework of linear stability theory. In other words, the family of these resolvent modes (high response) is highly linked to those series LANDO modes revealed in Sec. IV, which provide the majority of the contribution to the dynamics of TBL. Importantly, as these resolvent modes are featured by low frequency, the coherent structures of the modes are further illustrated as VLSMs. The high response of these modes in the STBLI flow then suggests the contribution of VLSMs to the low-frequency unsteadiness of the present STBLI flows.

VII. CONCLUSIONS

Following the idea of the previous work,[14] shock wave/boundary interaction flows can be classified into four scenarios according to the concept of noise amplifiers and oscillators from the dynamical system community. The present work investigates one of the scenarios in which the flow is incipiently separated with an incoming TBL. The absence of intrinsic instability in this configuration allows us to discuss the convective instability contributed by the incoming TBL.

Specifically, a supersonic turbulent flow over a compression ramp with a freestream Mach number of 2.95, a Reynolds number of 63 560, and a reflection angle of 15° is studied by using numerical simulations (LES), data-driven approaches (LANDO, SPOD), and theoretical methods (linear stability analysis). By analyzing and comparing these results, some significance of the STBLI flow dynamics is obtained and summarized as follows.

First, the present study identifies a family of coherent structures, which contributes to the dominant dynamics of motions in TBL. The dynamics of these structures satisfy a streamwise scale-frequency relation that $\Gamma = 0.78u_\infty/f$. The inverse relationship of the scale and

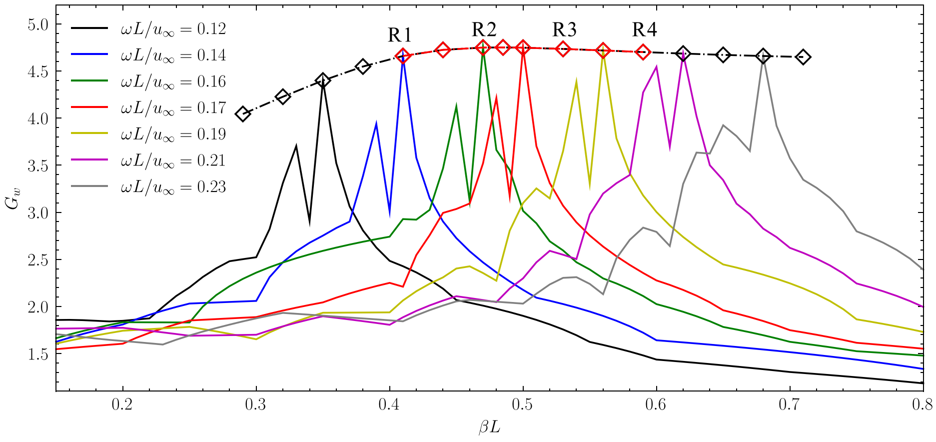

FIG. 11. Distribution of the premultiplied optimal gain as a function of the spanwise wavenumber. The solid lines indicate the distribution of the premultiplied gain with the fixed angular frequency. The diamonds represent the premultiplied optimal gain for each solid curve. Resolvent modes R1–R4 are evenly selected around the largest response with $\omega L/u_\infty$ of 0.14, 0.16, 0.18, and 0.20, respectively. These modes are shown in Fig. 12.

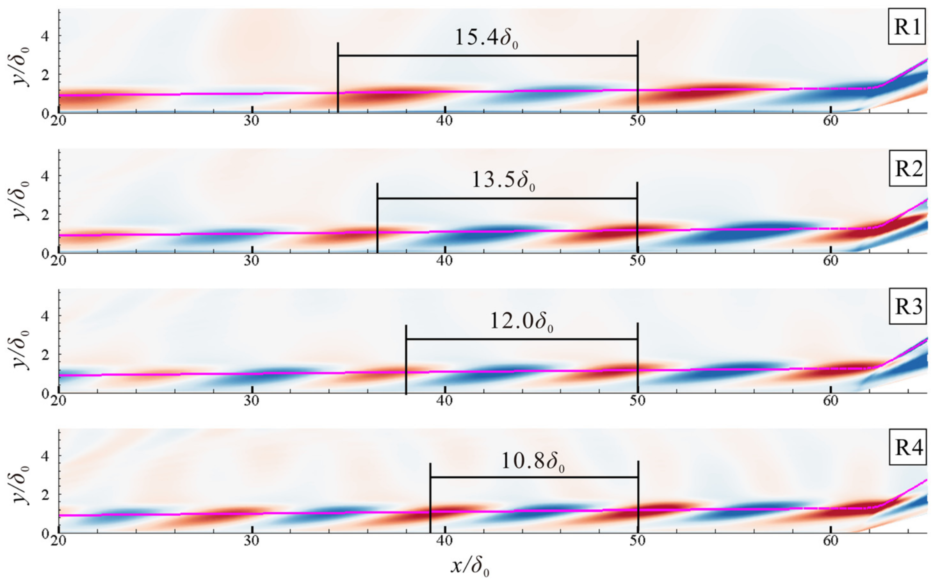

FIG. 12. The optimal response resolvent modes R1–R4 (see Fig. 11) of the streamwise velocity component with $\omega L/u_\infty$ of 0.14, 0.16, 0.18, and 0.20, respectively. The contour levels are evenly spaced between ± 0.4 of the maximum fluctuation. The magenta line is an iso-line of $0.99\,u_\infty$.

frequency suggests that the dynamics of VLSMs in TBL are featured by a low frequency.

Second, the dominant low frequency of the wall-pressure spectrum is identical to the frequency of the most energetic SPOD mode, and at the same time, the SPOD mode features VLSMs that satisfy the revealed streamwise scale-frequency relation. These consistencies suggest that the low-frequency unsteadiness is caused by the observed VLSMs from the family of coherent structures. A resolvent analysis is also performed to further demonstrate that the origins of the low-frequency dynamics of the present flow are from the VLSMs, which can be highly amplified by the forcing in the turbulent flow.

In fact, in the study by Hao,[13] the author has demonstrated that the low-frequency shock motion in STBLI can be caused by the excitation of an intrinsic mode by extrinsic disturbances in line with the mathematical models of Plotkin.[43] As a supplementary study to the work by Hao,[13] our attention is paid to the contribution of extrinsic disturbances to the low-frequency mechanism. The present study suggests that the extrinsic disturbances are likely to be the VLSMs in the TBL under the current flow conditions. The low-frequency motions of VLSMs convective from the upstream TBL interact with the following separated flow and result in the unsteadiness of STBLI flows featured by low frequency.

ACKNOWLEDGMENTS

The authors are grateful for the financial support provided by the Hong Kong Research Grants Council (Nos. 15217622 and 15204322).

AUTHOR DECLARATIONS

Conflict of Interest

The authors have no conflicts to disclose.

Author Contributions

Jianhui Fan: Conceptualization (equal); Data curation (equal); Formal analysis (equal); Investigation (equal); Methodology (equal); Writing – original draft (equal). **Jiaao Hao:** Conceptualization (equal); Funding acquisition (equal); Supervision (equal); Writing – review & editing (equal). **Chih-Yung Wen:** Conceptualization (equal); Funding acquisition (equal); Supervision (equal); Writing – review & editing (equal).

DATA AVAILABILITY

The data that support the findings of this study are available from the corresponding author upon reasonable request.

APPENDIX: VERIFICATION OF GRID INDEPENDENCE FOR RESOLVENT ANALYSIS

Figure 13 compares the optimal gains as a function of frequency ($\omega L/u_\infty$) with three different mesh configurations. The base flow for the resolvent analysis has a cell size of 1510 (streamwise direction) × 130 (wall-normal direction) for the present study and

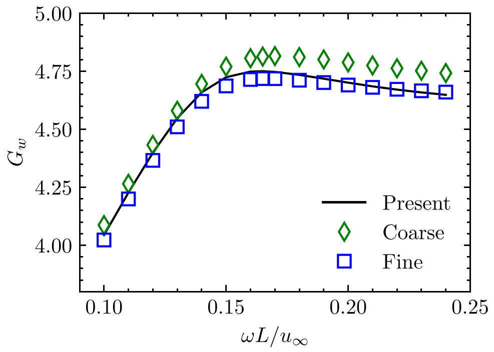

FIG. 13. The optimal gains as a function of frequency ($\omega L/u_\infty$) with various meshes. The black curve is the dashed curve shown in Fig. 11. The green diamonds and blue squares are the corresponding results of the coarse mesh and fine mesh, respectively.

has a cell size of 1200×100 for the coarse mesh and 1800×160 for the fine mesh. It is indicated by the figure that all of these three results have the highest response (gain) with $\omega L/u_\infty$ at 0.165. In addition, it is also noted that the results by the fine mesh only show a slight variation when compared with the results of the present mesh configuration. Further increasing the mesh resolution will not make a significant change in the results of the resolvent analysis.

REFERENCES

[1] N. Clemens and V. Narayanaswamy, "Low-frequency unsteadiness of shock wave/turbulent boundary layer interactions," Annu. Rev. Fluid Mech. **46**, 469–492 (2014).

[2] W. Hu, S. Hickel, and B. Van Oudheusden, "Low-frequency unsteadiness mechanisms in shock wave/turbulent boundary layer interactions over a backward-facing step," J. Fluid Mech. **915**, A107 (2021).

[3] J. Duan, X. Li, X. Li, and H. Liu, "Direct numerical simulation of a supersonic turbulent boundary layer over a compression–decompression corner," Phys. Fluids **33**(6), 065111 (2021).

[4] J. Poggie, N. Bisek, R. Kimmel, and S. Stanfield, "Spectral characteristics of separation shock unsteadiness," AIAA J. **53**(1), 200–214 (2015).

[5] S. Cao, J. Hao, I. Klioutchnikov, H. Olivier, and C. Wen, "Unsteady effects in a hypersonic compression ramp flow with laminar separation," J. Fluid Mech. **912**, A3 (2021).

[6] N. Hildebrand, A. Dwivedi, J. W. Nichols, M. R. Jovanovi, and G. V. Candler, "Simulation and stability analysis of oblique shock-wave/boundary-layer interactions at Mach 5.92," Phys. Rev. Fluids **3**, 013906 (2018).

[7] J. C. Robinet, "Bifurcations in shock-wave/laminar-boundary-layer interaction: Global instability approach," J. Fluid Mech. **579**, 85–112 (2007).

[8] Z. Song and J. Hao, "Global instability of the interaction between an oblique shock and a laminar boundary layer," Phys. Fluids **35**(8), 084121 (2023).

[9] G. S. Sidharth, A. Dwivedi, G. V. Candler, and J. W. Nichols, "Onset of three-dimensionality in supersonic flow over a slender double wedge," Phys. Rev. Fluids **3**(9), 093901 (2018).

[10] J. Hao, J. Fan, S. Cao, and C. Wen, "Three-dimensionality of hypersonic laminar flow over a double cone," J. Fluid Mech. **935**, A8 (2022).

[11] A. Dwivedi, G. Sidharth, J. W. Nichols, G. V. Candler, and M. R. Jovanović, "Reattachment streaks in hypersonic compression ramp flow: An input-output analysis," J. Fluid Mech. **880**, 113–135 (2019).

[12] J. Hao, S. Cao, P. Guo, and C. Wen, "Response of hypersonic compression corner flow to upstream disturbances," J. Fluid Mech. **964**, A25 (2023).

[13] J. Hao, "On the low-frequency unsteadiness in shock wave–turbulent boundary layer interactions," J. Fluid Mech. **971**, A28 (2023).

[14] J. Fan, J. Hao, and C. Wen, "Nonlinear interactions of global instabilities in hypersonic laminar flow over a double cone," Phys. Fluids **34**(12), 126108 (2022).

[15] K. M. Portera and J. Poggie, "Selective upstream influence on the unsteadiness of a separated turbulent compression ramp flow," Phys. Fluids **31**, 016104 (2019).

[16] A. Smits, B. McKeon, and I. Marusic, "High-Reynolds number wall turbulence," Annu. Rev. Fluid Mech. **43**, 353–375 (2011).

[17] B. Ganapathisubramani, N. Clemens, and D. Dolling, "Low-frequency dynamics of shock-induced separation in a compression ramp interaction," J. Fluid Mech. **636**, 397–425 (2009).

[18] R. Humble, G. Elsinga, F. Scarano, and B. van Oudheusden, "Three-dimensional instantaneous structure of a shock wave/turbulent boundary layer interaction," J. Fluid Mech. **622**, 33–62 (2009).

[19] B. Ganapathisubramani, N. Clemens, and D. Dolling, "Effect of upstream boundary layer on the unsteadiness of shock-induced separation," J. Fluid Mech. **585**, 369–394 (2007).

[20] J. H. Lee and H. J. Sung, "Very-large-scale motions in a turbulent boundary layer," J. Fluid Mech. **673**, 80–120 (2011).

[21] M. Guala, S. E. Hommema, and R. J. Adrian, "Large-scale and very-large-scale motions in turbulent pipe flow," J. Fluid Mech. **554**, 521–542 (2006).

[22] B. McKeon, A. Sharma, and A. Zheltovodov, "A critical-layer framework for turbulent pipe flow," J. Fluid Mech. **658**, 336–382 (2010).

[23] T. B. Davis, A. Uzun, and F. S. Alvi, "Optimal disturbances and large-scale energetic motions in turbulent boundary layers," J. Fluid Mech. **860**, 40–80 (2019).

[24] Y. Fan, W. Li, and R. D. Sandberg, "Resolvent-based analysis of hypersonic turbulent boundary layers with/without wall cooling," Phys. Fluids **35**(4), 045118 (2023).

[25] J. Fan, C. Uy, J. Hao, and C. Wen, "Coexistence of different mechanisms underlying the dynamics of supersonic turbulent flow over a compression ramp," Phys. Fluids **36**(1), 016115 (2024).

[26] J. Fan, J. Hao, C. Wen, and X. Xue, "Numerical investigation of supersonic flow over a parachute-like configuration including turbulent flow effects," Aerosp. Sci. Technol. **121**, 107330 (2022).

[27] J. Fan, J. Hao, C. Wen, and X. Xue, "Unsteady supersonic flows past two-body configurations with different separation distances," J. Aerosp. Eng. **36**(1), 04022109 (2023).

[28] Q. Hong, J. Hao, C. K. Uy, C. Wen, and Q. Sun, "Thermochemical nonequilibrium effects on high-enthalpy double-wedge flows," Phys. Fluids **34**, 063607 (2022).

[29] A. Zheltovodov, V. Trofimov, E. Schulein, and V. Yakovlev, "An experimental documentation of supersonic turbulent flows in the vicinity of forward- and backward-facing ramps," Inst. Theor. Appl. Mech., USSR Acad. Sci, Novosibirsk, Tech. Rep. No. 2030, 1990.

[30] H. Choi and P. Moin, "Grid-point requirements for large eddy simulation: Chapman's estimates revisited," Phys. Fluids **24**(1), 011702 (2012).

[31] M. Klein, A. Sadiki, and J. Janicka, "A digital filter based generation of inflow data for spatially developing direct numerical or large eddy simulations," J. Comput. Phys. **186**(2), 652–665 (2003).

[32] E. R. Van Driest, "Turbulent boundary layer in compressible fluids," J. Aeronaut. Sci. **18**(3), 145–160 (1951).

[33] P. J. Baddoo, B. Herrmann, B. J. McKeon, and S. L. Brunton, "Kernel learning for robust dynamic mode decomposition: Linear and nonlinear disambiguation optimization," Proc. Math. Phys. Eng. Sci. **478**(2260), 20210830 (2022).

[34] J. del Álamo and J. Jimenez, "Linear energy amplification in turbulent channels," J. Fluid Mech. **559**, 205–213 (2006).

[35] C. Chi, D. Thévenin, A. J. Smits, S. Wolligandt, and H. Theisel, "Identification and analysis of very-large-scale turbulent motions using multiscale proper orthogonal decomposition," Phys. Rev. Fluids **7**(8), 084603 (2022).

[36] W. Zhu, X. Chen, and L. Fu, "Resolvent analyses of incompressible turbulent channel, pipe and boundary-layer flows," Int. J. Heat Fluid Flow **106**, 109331 (2024).

[37] J. Zhou, R. J. Adrian, S. Balachandar, and T. Kendall, "Mechanisms for generating coherent packets of hairpin vortices in channel flow," J. Fluid Mech. **387**, 353–396 (1999).

[38] R. Deshpande, C. Silva, and I. Marusic, "Evidence that superstructures comprise self-similar coherent motions in high Reynolds number boundary layers," J. Fluid Mech. **969**, A10 (2023).

[39] K. Taira, S. L. Brunton, S. T. Dawson, C. W. Rowley, T. Colonius, B. J. McKeon, O. T. Schmidt, S. Gordeyev, V. Theofilis, and L. S. Ukeiley, "Modal analysis of fluid flows: An overview," AIAA J. **55**(12), 4013–4041 (2017).

[40] J. L. Lumley, "The structure of inhomogeneous turbulent flows," in *Atmospheric Turbulence and Radio Wave Propagation*, edited by A. M Yaglom and V. I. Tatarskii (Nauka, Moscow, 1976), pp. 166–178.

[41] J. L. Lumley, "Stochastic tools in turbulence," J. Fluid Mech. **41**, 413–415 (1970).

[42] B. T. Chu, "On the energy transfer to small disturbances in fluid flow (Part I)," Acta Mech. **1**(3), 215–234 (1965).

[43] K. Plotkin, "Shock wave oscillation driven by turbulent boundary layer fluctuations," AIAA J. **13**(8), 1036–1040 (1975).